J Oceanogr (2015) 71:409–425
DOI 10.1007/s10872-015-0301-9

ORIGINAL ARTICLE

Vertical and horizontal structures of the North Pacific subtropical gyre axis

Masafumi Kimizuka[1] · Fumiaki Kobashi[1,2] · Atsushi Kubokawa[3] · Naoto Iwasaka[1]

Received: 16 January 2014 / Revised: 31 March 2015 / Accepted: 17 May 2015 / Published online: 28 May 2015

Abstract Mean structures of the North Pacific subtropical gyre are investigated using Argo float observations and several wind stress products, with a particular focus on the gyre axis, which is defined as a large-scale boundary between eastward motions on the northern part of the subtropical gyre and westward motions on the southern part. Structures of the gyre axis are different between the regions east and west of about 180°. In the west, the gyre axis is affected by the strong Kuroshio Extension jet, showing discrepancy with features expected from the Sverdrup balance and ventilated thermocline theory. In the east, depth-integrated geostrophic circulation displays the two gyre axes at about 25°N and 30°N in association with a local cyclonic wind stress curl anomaly. It is expected from the Sverdrup balance that the two gyre axes would extend to the west across the subtropical gyre, but the actual geostrophic circulation exhibits only one gyre axis around 30°N to the west. The vertical structure of the subtropical gyre exhibits a remarkable northward shift of the gyre axis with depth in the east, consistent with the southward decrease in the thickness of density layers around the gyre axis, while the northward shift is less obvious in the west, where the gyre axis lies along the southern flank of the Kuroshio Extension. The gyre shift is relatively smaller in the central mode water (CMW) layer due to the horizontal uniformity of the CMW, suggesting a dynamic effect of the CMW on large-scale circulations of the subtropical gyre.

Keywords North Pacific subtropical gyre · Wind-driven circulation · Gyre axis · Sverdrup balance · Ventilated thermocline theory

1 Introduction

The subtropical gyre of the North Pacific is a large-scale anticyclonic circulation between approximately 15°N and 45°N. It is basically driven by the northeast trade winds and the westerlies, as explained by a classical wind-driven circulation theory that was developed by some pioneering work by Sverdrup (1947), Stommel (1948) and Munk (1950). Sverdrup (1947) showed the Sverdrup balance in the interior ocean, where depth-integrated geostrophic circulations are related to surface wind stress curl. The Sverdrup circulation is set up by barotropic Rossby waves propagating across the ocean.

The validity of the Sverdrup balance was investigated in the North Pacific by Hautala et al. (1994), who analyzed ship-observed surface wind and hydrographic observations of a zonal section along 24°N and showed that the Sverdrup balance is almost valid in the entire ocean basin. Their results were further confirmed by Aoki and Kutsuwada (2008) from an analysis of several different wind stress products and historical hydrographic data. Since the barotropic adjustment time is less than one month for the North Pacific subtropical gyre, the circulation is considered to equilibrate with wind forcing on seasonal and longer time scales. The time-varying Sverdrup balance has also been examined by a number of studies (e.g., Sekine and

✉ Masafumi Kimizuka
d122006@kaiyodai.ac.jp

[1] Graduate School of Marine Science and Technology, Tokyo University of Marine Science and Technology, Etchujima 2-1-6, Koto-Ku, Tokyo 135-8533, Japan

[2] Research Institute for Global Change, Japan Agency for Marine-Earth Science and Technology, Yokosuka, Japan

[3] Faculty of Environmental Earth Science, Hokkaido University, Sapporo, Japan

Kutsuwada 1994; Kubota et al. 1995; Chelton and Mestas-Nuñez 1996).

While the Sverdrup theory provided a basic picture of barotropic wind-driven circulation, the ventilated thermocline theory (Luyten et al. 1983) and the theory of the potential vorticity (PV) homogenization for an unventilated thermocline (Rhines and Young 1982; Young and Rhines 1982) brought insights on the baroclinic structure of the ocean. From an observational point of view, large-scale aspects of structures of geostrophic circulation were examined in the North Pacific subtropical gyre by Qu (2002). He defined the axis of the subtropical gyre as the meridional maximum of depth-integrated dynamic height and Sverdrup transport using climatologies from World Ocean Atlas 1998 and Hellerman and Rosenstein's (1983) surface wind. Their axes both appear along 30°N and extend almost zonally, showing a good agreement in position. He further examined the vertical structure of the axis from dynamic heights at each depth, reporting that the gyre axis gradually moves poleward, from 25°N at 100 m to 38°N at 800 m depth in the central and eastern basin east of 180°, but in the west it does not change significantly and almost stays at 30°N. The northward shift of the gyre has also been reported by other observational studies (Reid and Arthur 1975; Huang and Qiu 1994; Kobashi et al. 2006) and numerical models (Nakano and Suginohara 2002). Because the northward shift of the gyre is essentially related to β-spiral caused by the conservation of PV of the gyre circulation (Stommel and Schott 1977), it is a crucial characteristic of the ventilated thermocline theory. Nevertheless, the relationship between the gyre shift and the structure of PV has not yet been investigated in detail from observations.

The northward shift of the gyre is considered as a key structure for the formation of the eastern Subtropical Countercurrent (STCC), which is a shallow eastward current around 26°N between 180° and 160°W (Kobashi et al. 2006). The eastern STCC is basically maintained by the central mode water (CMW), a vertically homogeneous water mass characterized by low PV in the central subtropical gyre (Nakamura 1996; Suga et al. 1997). The CMW forms in wintertime deep mixed layer near the Kuroshio Extension, subducted into the thermocline and advected by gyre circulation. Lighter and denser parts of the CMW diverge from the formation site and circulate along the inner and outer paths of the subtropical gyre, respectively, due to the northward retreat of the gyre of denser isopycnals (Oka and Suga 2005; Kobashi et al. 2006). They again encounter in the central subtropical gyre, piling up in the vertical and forming a low PV pool (Kubokawa 1999; Kubokawa and Inui 1999). This pool can heave an overlying thermocline, causing subsurface temperature fronts and thus generating shallow STCC through the thermal wind relation. The STCC is known to affect surface winds and precipitation through its thermal effects (Kobashi et al. 2008; Xie et al. 2011). Detailed knowledge of structure of the subtropical gyre would help to understand variability of STCC and its influences on the atmosphere (Kobashi and Kubokawa 2012).

The present study examines the mean structures of the North Pacific subtropical gyre with a particular focus on the gyre axis, using Argo float observations and wind stress data from several reanalysis and satellite products. We describe the gyre axis in a different way from Qu (2002), to show a detailed picture of the gyre axis and its relationship with the Sverdrup balance and the ventilated thermocline theory. Our study identifies differences between the regions east and west of about 180°. Distinct from the west where the gyre axis is strongly affected by the Kuroshio Extension jet and its recirculation gyre, the east shows some consistency with features expected from the Sverdrup balance and the ventilated thermocline theory. We find two gyre axes in the east that are associated with a local cyclonic wind stress curl anomaly. We also show that a northward shift of the gyre axis with depth, which is a prominent feature in the east as shown by Qu (2002), occurs non-uniformly in the vertical, due to the presence of the CMW and the pycnocline. The results present an important dynamic effect of the CMW on large-scale circulations of the subtropical gyre.

The rest of this paper is organized as follows. Section 2 describes the data used and the method employed to determine the gyre axis. In Sect. 3, the relationship between the wind-driven Sverdrup circulation and the depth-integrated geostrophic circulation is first shown, and then the vertical structure of the gyre axis is examined. Section 4 provides a summary and discussion.

2 Data and methods

2.1 Geostrophic circulation

This study uses monthly temperature and salinity data from 2001 to 2011 from grid point values of the monthly objective analysis using Argo float data (MOAA GPV) produced by Hosoda et al. (2008). This product is based on Argo float data, the triangle trans-ocean buoy network (TRITON) and available conductivity-temperature-depth (CTD) profilers, optimally interpolated at standard pressure levels from 10 to 2000 dbar on a 1° grid in space.

Dynamic heights are calculated at each depth referenced to 2000 dbar from the monthly MOAA GPV. For the comparison with geostrophic transports expected from surface wind stress curl, depth-integrated dynamic heights are also computed by integrating dynamic heights between the surface and 2000 dbar. These maps of dynamic heights are all smoothed with a 13-month running mean to remove

Table 1 Summary of the information for each wind stress data set used in the present study

Data set	Type	Analysis period	Spatial resolution
JRA	Reanalysis	Jan 2001–Dec 2011	T106 Gaussian grid (approximately 1.125°)
J-OFURO	Satellite observations	Jan 2001–Dec 2008	1°
NCEP1	Reanalysis	Jan 2001–Dec 2011	T62 Gaussian grid (approximately 1.9°)
NCEP2	Reanalysis	Jan 2001–Dec 2011	T62 Gaussian grid (approximately 1.9°)
MERRA	Reanalysis	Jan 2001–Dec 2011	½° latitude × 2/3° longitude
HR	Ship observations	Monthly climatology from 1890 to 1976	2°

seasonal variations, and then are used to obtain geostrophic velocity. Note that our results are not sensitive to the choice of reference level. If another commonly used level of 1000 dbar is adopted, our results do not change significantly (not shown).

The Argo float observations in the North Pacific are quite sparse until 2004, and thus the MOAA GPV before 2005 is considered to be almost the same as the World Ocean Atlas climatology that is a first-guess value in the optimal interpolation (Hosoda et al. 2008). We conducted the same analysis using the data from 2005 to 2011, and found that the distribution of the gyre axis is almost the same as those from 2001 to 2011.

2.2 Wind-driven transport

We analyzed six products of monthly mean surface wind stress data: Japanese 25-year Reanalysis (JRA; Onogi et al. 2007), Japanese Ocean Flux Data Sets with Use of Remote Sensing Observations (J-OFURO; Kubota et al. 2002), National Centre for Environmental Prediction (NCEP)/National Center for Atmospheric Research (NCAR) reanalysis (NCEP1; Kalnay et al. 1996), NCEP/Department of Energy (DOE) reanalysis (NCEP2; Kanamitsu et al. 2002), the Modern-Era Retrospective Analysis for Research and Applications (MERRA; Rienecker et al. 2011) and Hellerman and Rosenstein's (1983) data (HR). The period analyzed in this study is the same as that of the MOAA GPV, but the J-OFURO covers only from 2001 to 2008 and the HR is monthly climatology from 1870 to 1976. The JRA covers the period until 2004, but continues to be updated for the subsequent period using the same assimilation system, the Japan Meteorological Agency (JMA) Climate Data Assimilation System (JCDAS). The specifications of the products are summarized in Table 1.

Sverdrup balance in response to surface Ekman convergence is expressed as

$$\int_{x_e}^{x}\int_{-h}^{0} v_G \,dz\,dx = \frac{f}{\beta}\int_{x_e}^{x} w_{EK}\,dx, \tag{1}$$

where x_e is the eastern boundary, v_G is the meridional geostrophic velocity at each depth, f is the Coriolis parameter, β is the meridional gradient of the Coriolis parameter, h is the depth of wind-driven flow, and w_{EK} is the Ekman pumping velocity. Here we assume that vertical velocity at a depth of bottom of wind-driven flow is negligible. This equation is rewritten by substituting the Ekman pumping velocity $[w_{EK} = \mathbf{k}\cdot\nabla\times(\boldsymbol{\tau}/f\rho)]$ as

$$\int_{x_e}^{x}\int_{-h}^{0} v_G \,dz\,dx = \frac{1}{\beta\rho}\int_{x_e}^{x} \mathbf{k}\cdot\nabla\times\boldsymbol{\tau}\,dx + \frac{1}{f\rho}\int_{x_e}^{x}\tau^x\,dx, \tag{2}$$

where ρ is the density, $\boldsymbol{\tau}$ is the wind stress vector $\boldsymbol{\tau} = (\tau^x, \tau^y)$, and $\mathbf{k}$ is a unit vector in the local vertical direction. In this study, we calculate the geostrophic transport from the right-hand side of Eq. (2), which we will refer to as the wind-driven transport, following the term used by Aoki and Kutsuwada (2008). We also henceforth refer to the circulation associated with the wind-driven transport as the wind-driven circulation.

The Ekman pumping velocity is smoothed in space and time. The MOAA GPV used to derive geostrophic circulation is spatially smoothed by an optimal interpolation with a meridional decorrelation scale of about 3°–4° around 30°N at depths of 200–400 m (Hosoda et al. 2008), though it is slightly different at locations and depths. To match the resolution, the monthly Ekman pumping velocity, except for that from relatively coarse-resolution NCEP1, NCEP2 and HR, is smoothed meridionally by a 3° moving average. This procedure filters out features with scales less than about 300 km. Then, the monthly maps of the wind-driven transport are smoothed with the 13-month running mean to remove seasonal variations. Regarding the HR, we look at only annual mean wind-driven transport.

2.3 Gyre axis

In this study, the gyre axis is defined as the large-scale boundary between eastward motions on the northern part of the subtropical gyre and westward motions on the southern part. The gyre axis is calculated from maps of geostrophic circulation and wind-driven transport.

The climatological positions of the gyre axis, which are the main target of the present study, are determined from

the rate of appearance of the gyre axis. The gyre axis is first detected from each monthly map and then it is counted at each grid over the analysis period, which will be shown as the percentage. We regard a band with the high percentage as the climatological gyre axis. It should be noted that this climatological gyre axis does not necessarily correspond to a boundary between eastward motions to the north and westward motions to the south at the time mean maps. We will make a brief comparison with the gyre axis of the time mean maps. Because it is long-term mean data (Table 1), for wind-driven transport calculated from the HR, the gyre axis is calculated only from the mean map.

In comparison with Qu (2002), who defined the gyre axis as the meridional maximum of mean Sverdrup transport and dynamic heights, the present study cannot exclude the existence of multiple axes, and thus may be able to capture the structure of the subtropical gyre in detail.

The result, however, should be carefully discussed, because our method is sensitive to tiny spatial variations of zonal velocity and transport. The present study assessed the statistical significance of the climatological gyre axis. By adopting the bootstrap method (Press et al. 1992), we generated 1000 maps of the appearance rate of the gyre axis. At each grid point, we first merged the time series of zonal velocity/transport with those from two meridionally adjacent grid points, which are used to define the gyre axis at each map, and then resampled the data to make 1000 data sets using the bootstrap technique on the assumption that all the data are independent. Using this new data, we calculated the appearance rate of the gyre axis in the same way from each data set, and then determined the 95th and 90th percentile confidence levels. We checked if the appearance rate from the original data exceeded the confidence levels at each grid.

In addition to the statistical assessment, we looked at the effect of small-scale variations such as eddies on the climatological gyre axis. To highlight large-scale structures of zonal velocity/transport, we calculated the gyre axis from a polynomial curve fitting to the monthly meridional profiles and then determined the climatological gyre axis. We will compare the result with the original one.

Although the climatological gyre axis in the present study has some weakness as mentioned above, the statistical assessment and the additional analysis will support the meaningfulness of our gyre axis. We believe that the gyre axis is useful for describing structures of ocean circulation.

3 Results

3.1 Depth-integrated circulation

Figure 1 shows the mean depth-integrated dynamic height and the rate of the appearance of the gyre axis. In the western basin, the climatological gyre axis is recognized from a zonal band of significant high percentages along about 30°N. The location of the gyre axis is consistent with the result of Qu (2002). On the other hand, in the east of 170°W, there are two meridional mounds of high percentages around 25°N and 30°N, suggesting two gyre axes. These two gyre axes are significant at the 95th percentile confidence level. The northern axis looks like it is connected to the western gyre axis. Although these two gyre axes may be obscure in the mean depth-integrated dynamic height map, the depth-integrated dynamic height tends to

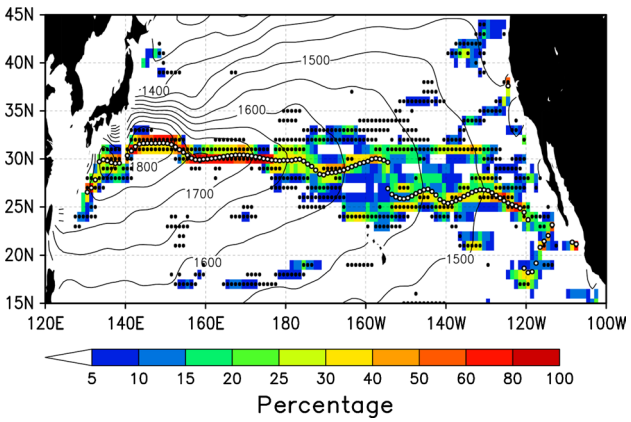

Fig. 1 Mean depth-integrated dynamic height (m^2) and the rate of appearance of the gyre axis (*color*). *Open circles* denote the position of the gyre axis determined from the mean depth-integrated dynamic height. *Black dots* denote the grid points where the appearance rate of the gyre axis is statistically significant at the 95th percentile confidence interval

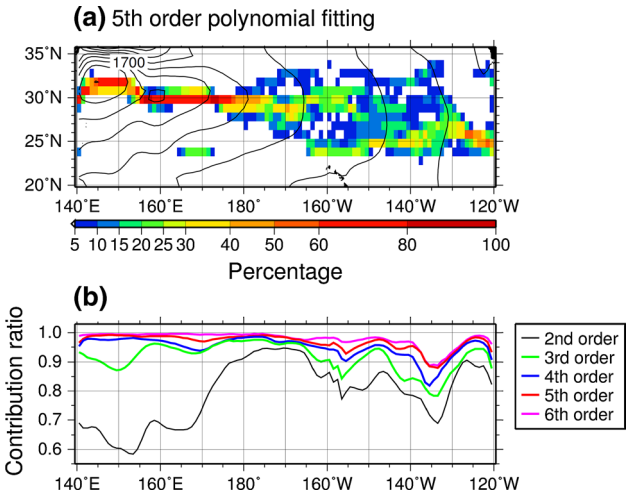

Fig. 2 **a** Same as in Fig. 1, but calculated from a fifth order polynomial curve fitting to a monthly meridional profile of the depth-integrated dynamic height in the latitude range of 20°–35°N at each longitude, and **b** the mean contribution ratio of each fitting of second to sixth order polynomials at each longitude (see the text for details)

have some local peaks or be uniform in the meridional direction, and therefore the axis defined from the mean map (marked by open circle symbols in Fig. 1) displays one gyre axis with somewhat unnatural discontinuity around 155°W.

As in Fig. 1, Fig. 2a shows the appearance rate of the gyre axis, but calculated from a fifth order polynomial curve fitted to a monthly meridional profile of depth-integrated dynamic heights in the latitude range of 20°–35°N at each longitude, in order to highlight large-scale structures. Figure 2b indicates the mean contribution ratio, which represents the extent to which each fitting of second to sixth order polynomials explains the original profile of depth-integrated dynamic heights. As seen from Fig. 2a, the polynomial fitting can capture almost the same two gyre axes between 165°W and 150°W, as in Fig. 1. They are obvious from the fitting with more than fourth order polynomials (not shown). The northern axis, however, disappears to the east of 150°W, where the contribution ratio decreases slightly to the east (Fig. 2b), suggesting the importance of higher-order terms there. Because the appearance rate of the gyre axis from the original data is statistically significant there (Fig. 1), the northern axis east of 150°W may be associated with relatively small-scale but persistent geostrophic circulation.

The existence of the two gyre axis in the east is also supported by the relative vorticity calculated from a depth-averaged mean geostrophic velocity between the surface and 2000 m. Figure 3 shows the zonal averages of the relative vorticity between 165°W and 130°W, revealing significant cyclonic rotation anomaly with positive curl around 28.5°N between the two gyre axes, embedded in the background of basin-scale anticyclonic circulation of the subtropical gyre.

The two climatological gyre axes are also seen from the wind-driven transport, with some notable differences. Figure 4 shows the mean wind-driven transport and the appearance rate of the gyre axis. The MERRA that has the most fine grid interval (Table 1) displays several bands of high percentage (Fig. 4e). The two high-percentage bands are evident around 26°N and 32°N. They extend from off the west coast of the North America to the west across the basin, and seem to merge together near 140°E. These two bands are also seen roughly from the gyre axis calculated from the mean wind-driven transport map (not shown). Figure 5 shows the percentile of the appearance rate of the gyre axis, which was assessed from the bootstrap method (Sect. 2.3). The southern band around 26°N is significant at the 90th percentile confidence level. The northern band is also significant to the east of 170°W, mostly at the 90th percentile confidence level, though the percentile decreases to about 50–75th percentile to the west. The low percentile in the west could imply high variability of the gyre axis within the band. The two bands are also obvious from the

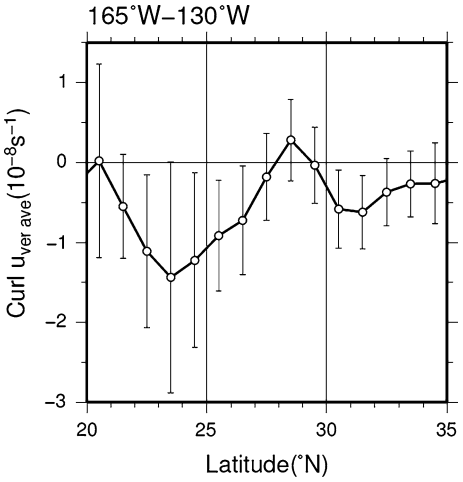

Fig. 3 Relative vorticity of the depth-averaged geostrophic velocity between the surface and 2000 m, zonally averaged between 165°W and 130°W. The *error bars* denote the standard deviation

appearance rate map calculated from a fourth order polynomial fitting (not shown).

These two bands are common in the J-OFURO (Fig. 4b), and are partly identifiable from the JRA and the lower-resolution NCEP1 and NCEP2 (Fig. 4a, c, d), though their latitudinal positions are slightly different, probably due to the different grid spacing (Table 1). In the J-OFURO (Fig. 5b), the northern band shows a percentile of about 70-90 around 30°N to the west of 155°W. The northern band in the JRA is mostly significant at the 80th percentile confidence level, except in the area between 180° and 145°W (Fig. 5a). The NCEP1 and NCEP2 display a high percentile exceeding 90 at the northern band around 33°–34°N. In addition, as shown by Qu (2002), the northern band is also evident from the mean map of the HR (Fig. 4f). These features may support the existence of the northern band.

The southern band from the J-OFURO, JRA, NCEP1 and NCEP2 is overall significant at the confidence levels between the 80th and 95th percentiles (Fig. 5). There are some noticeable differences in distribution. The southern band east of 155°W is found around 22.5°N in the JRA and NCEP2, located further to the south as compared to that of the MERRA. A similar southern band is also seen in the HR, which might result from the contamination of the band around 26°N and another southeast-slanted band extending from 24°N to 19°N in the MERRA (Fig. 4e).

These discrepancies among the data sets might be attributable to various factors such as the differences in resolution and assimilation method adopted by the reanalysis products and what kind of observation data they used, but identifying their causes is beyond the scope of this study. Although there are discrepancies among the data sets, all the products strongly suggest that wind over the North

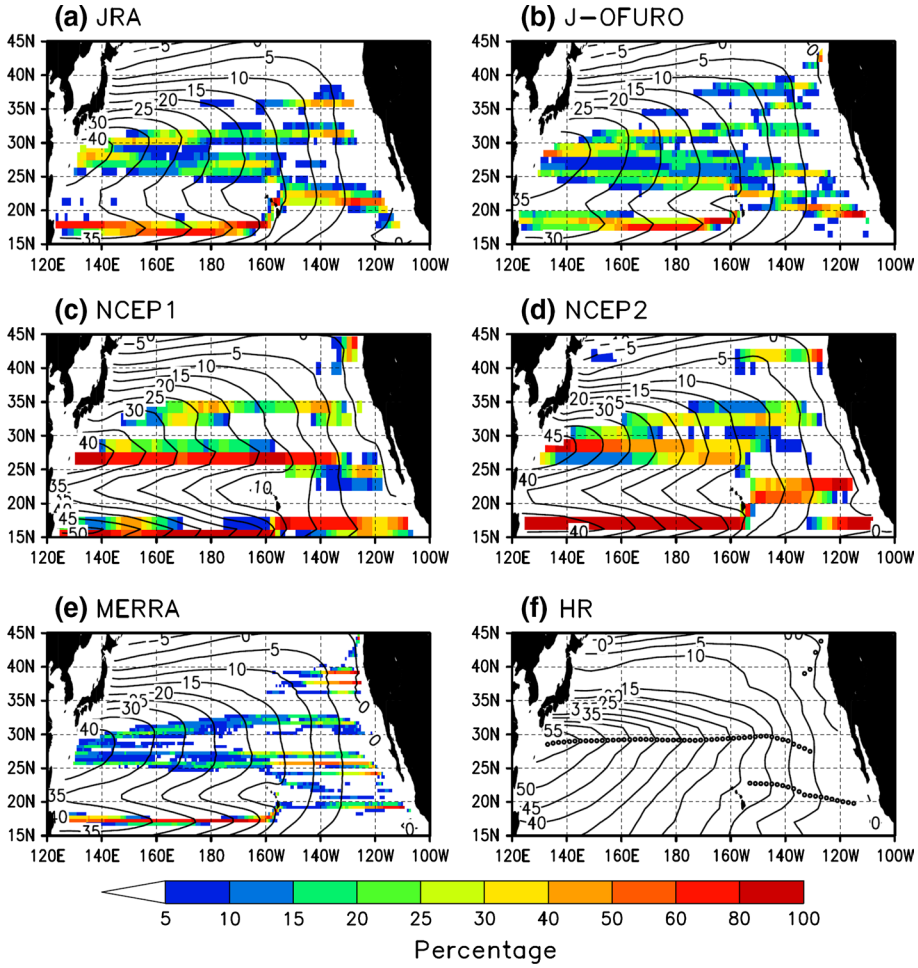

Fig. 4 Mean wind-driven transport (Sv) and the rate of appearance of the gyre axis (*color*), calculated from **a** JRA, **b** J-OFURO, **c** NCEP1, **d** NCEP2, **e** MERRA and **f** HR. *Open circles* in **f** denote the position of the gyre axis determined from the mean wind-driven transport

Pacific tends to produce two gyre axes in the wind-driven circulation, so we consider that they would deserve to be compared with the ocean gyre axis calculated from the gridded Argo data.

Other bands of high percentages are seen from the MERRA near 35°–40°N to the east of 155°W and near 17°N to the west of the Hawaiian Islands. The similar bands may be recognized from the other data sets except for the HR. The first bands east of 155°W are located at the northeast corners of the subtropical gyres. The second band is associated with a local response of wind stress curl to the Hawaiian Islands (Xie et al. 2001). Therefore, these bands are considered distinct from a large-scale gyre axis of the subtropical gyre, which is the target of the present study.

Figure 6 shows histograms of the appearance rate of the gyre axis against latitude, zonally averaged between 150°E and 170°E and 170°W and 150°W, together with the zonal averages of the depth-integrated dynamic height (Fig. 6a, b) and wind-driven transports (Fig. 6c–l). In the eastern basin (Fig. 6b, d, f, h, j, l), the two peaks of the appearance rate in the depth-integrated dynamic height around 25°N and 30°N are roughly collocated with those of the wind-driven transports from the JRA, J-OFURO and MERRA, though the ocean gyre axes both lie slightly to the south. The collocation of the two gyre axes indicates a good correspondence between geostrophic circulation and wind-driven circulation.

In the western basin, except for the NCEP1, the gyre axes of the depth-integrated dynamic height and the wind-driven transports are commonly present at the same latitude around 30°N, where their zonal averages both show a meridional peak (Fig. 6a, c, e, g, i, k). The wind-driven transport from the JRA and the J-OFURO as well as the MERRA shows another peak of the percentage around 26°N, as seen from Fig. 4, but there seems to be no ocean gyre axis equivalent to it, suggesting some discrepancy with the wind-driven circulation.

The rate of appearance of the gyre axis does not necessarily indicate that the two gyre axes exist at the same time. Although the temporal variability of the gyre axes is beyond the purpose of the present study, we briefly examined the rate of appearance of the northern (southern) gyre axis, by counting at each longitude from the monthly maps if there is at least one gyre axis between 23°N (28°N) and

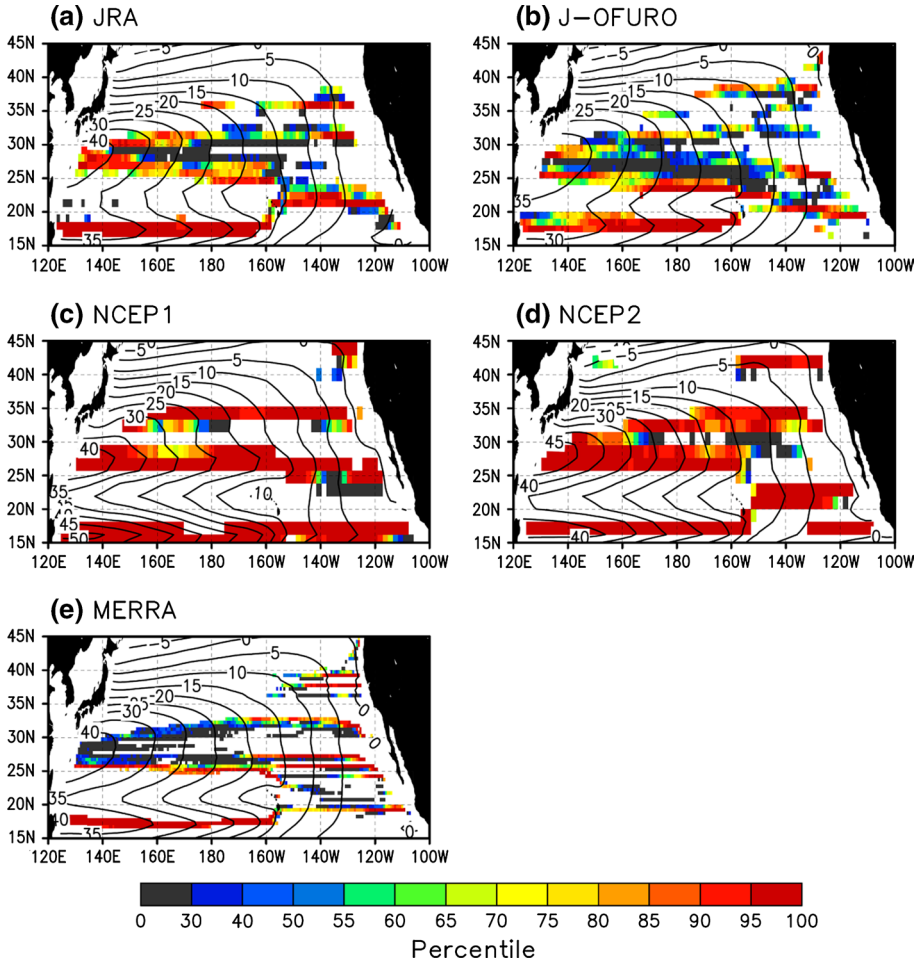

Fig. 5 Percentile of the rate of appearance of the gyre axis among 1000 appearance rate maps generated by the bootstrap method (see the text for detail), for **a** JRA, **b** J-OFURO, **c** NCEP1, **d** NCEP2 and **e** MERRA, shown only at the grid points with the appearance rate more than 5 % in Fig. 4. *Contours* are the mean wind-driven transport (Sv), the same as in Fig. 4

28°N (33°N) for the depth-integrated dynamic heights and between 24°N (29°N) and 29°N (34°N) for the MERRA-derived wind-driven transports (not shown). The results show that the percentage of all the gyre axes exceeds 50 % in the region east of 165°W. The zonally averaged percentages of the northern and southern gyre axes between 165°W and 140°W are 62 and 69 % for ocean geostrophic circulation and 64 and 77 % for wind-driven circulation, respectively. These rates are roughly comparable to each other between geostrophic circulation and wind-driven circulation.

What causes the two gyre axes in the eastern basin? Figure 7 shows the mean maps of wind-driven transport, Ekman pumping velocity and wind stress vector from the MERRA. The Ekman pumping velocity is relatively weak around 125°W between the two gyre axes at 25°N and 32°N, suggesting a cyclonic anomaly of wind stress curl. The high-pass filtered maps with a running average of 10° width (Fig. 7b) clearly show a cyclonic wind anomaly with a positive Ekman pumping velocity anomaly. It has a center around 125°W, and extends with weak cyclonic anomalies to the west around 150°W. This cyclonic wind anomaly is responsible for the formation of the two gyre axes across the subtropical gyre, because if we calculate the wind-driven transport by integrating Eq. (2) from 160°W instead of the eastern boundary, the two gyre axes disappear, but one gyre axis remains at around 30°N (not shown).

The area of the cyclonic wind anomaly is dominated by northeasterly winds blowing from the subtropical high (Fig. 7a). High-passed wind stress vectors (Fig. 7b) indicate that the cyclonic wind curl anomaly is maintained by local southeasterly wind anomalies, which are probably associated with local weakening of the northeasterly winds. These features are common in the JRA and J-OFURO (not shown).

3.2 Vertical structure of geostrophic circulation

In this subsection, we investigate how the gyre axis of geostrophic circulation changes in position with depth, and then show how these changes are related to density structures of the subtropical gyre.

Figure 8 shows the mean dynamic heights and acceleration potentials together with the appearance rate of the gyre

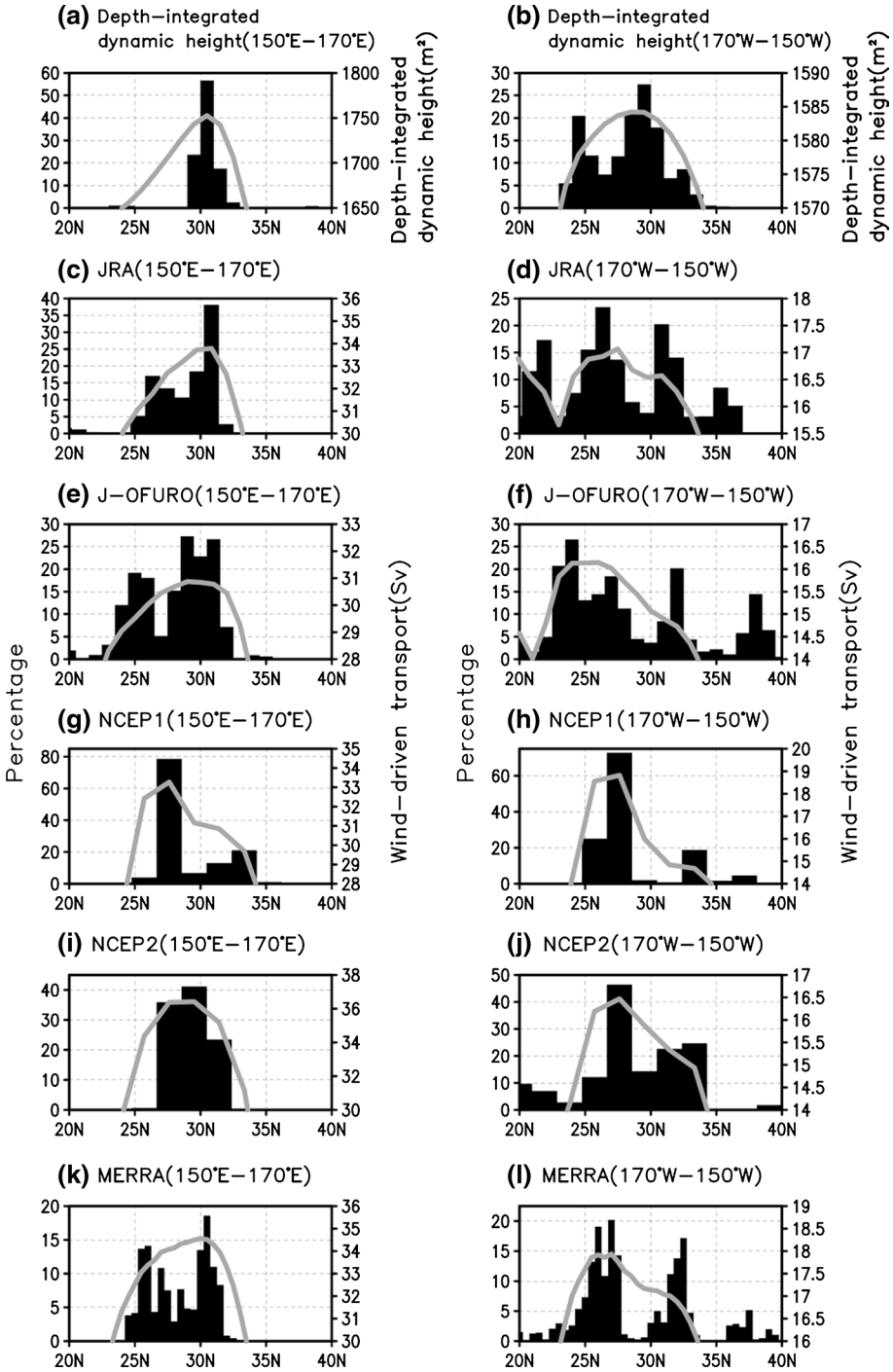

Fig. 6 Rates of appearance of the gyre axis of (**a**, **b**) depth-integrated dynamic height and (**c**–**l**) wind-driven transport, averaged between 150°E and 170°E (*left*), and between 170°W and 150°W (*right*). *Gray curves* denote the zonal mean values in each longitudinal range

axis at different depths and isopycnal surfaces. The distribution of the appearance rate of the gyre axis is nearly unchanged even if it is calculated from fourth-order polynomial fitting maps (not shown). The thick black line represents the climatological gyre axis, which basically traces the significant meridional peak of the high appearance rate of the gyre axis, with zonal continuity taken into consideration between 140°E and 140°W. As shown later, the climatological gyre axis nearly agrees with the gyre axis based on the time mean map. The northward shift of the gyre axis with depth is quite obvious. Consistent with the results of Qu (2002), the northward shift occurs markedly to the east of 180°, where the gyre axis moves to the north by more than 10° from 100 to 800 m depths, while to the west it does not change significantly with depth and lies around 30°N at almost the same latitude of the gyre axis of the depth-integrated geostrophic circulation. These features are also evident on isopycnal surfaces (Fig. 8d–f).

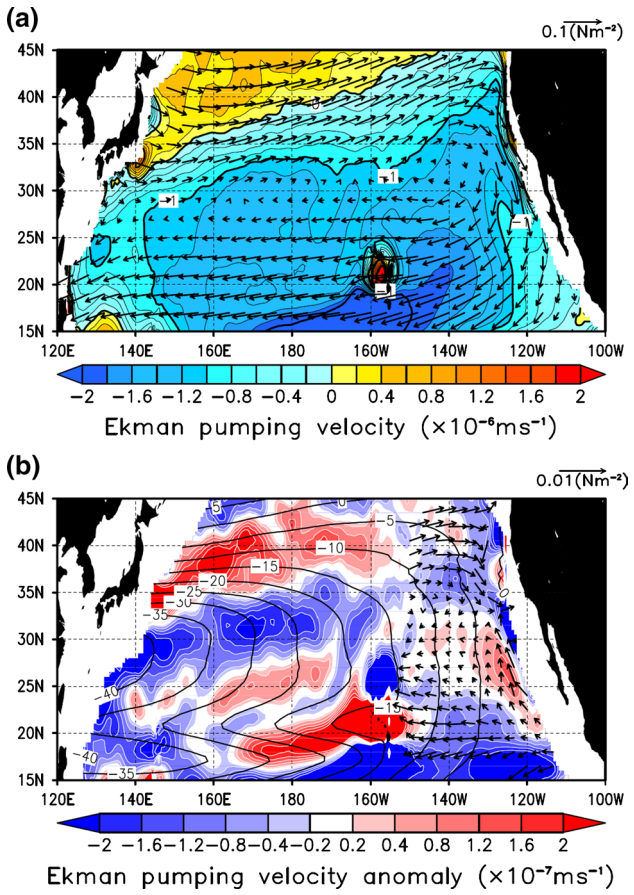

Fig. 7 **a** Ekman pumping velocity (w_{EK}) and wind stress vector from the MERRA, and **b** their anomalies obtained by a meridional high-pass filter. The wind stress vector anomaly is shown only for the east of 150°W. *Black contours* in the *lower panel* indicate the mean wind-driven transport

At a depth of 100 m, some significant bands with high percentage of the gyre axis are discernible around 18°N and 23°N in the western basin (Fig. 8a). They appear along the southern boundary of narrow eastward jets of the Hawaiian Lee Countercurrent (e.g., Qiu et al. 1997; Flament et al. 1998; Xie et al. 2001) and the northern Subtropical Countercurrent (e.g., Uda and Hasunuma 1969; Kobashi et al. 2006). Because these jets are narrow and distinct from large-scale eastward motions of the subtropical gyre, they are not regarded as the gyre axis in the present study.

At a depth of 500 m and a density surface of 1026.5 kg/m^3 (Fig. 8b, e), two bands of high percentage may be identified along about 27°N and 32°N to the east of 155°W. The northern band is an eastern part of the band extending from the west. As the northern band moves northward with depth, the southern band also seems to shift to the north around 33°N at 800 m depth and 1027.2 kg/m^3 density surface (Fig. 8c, f), though it is not clear compared to the northern band. The two bands might be indicative of the relationship with those of the depth-integrated geostrophic circulation in the east. However, because the circulation at each depth level does not necessarily correspond to the depth-integrated circulation, further study will need to address their relationship. The present study focuses on the northern higher-percentage band. Some patchy high percentage areas are found south of 25°N at the deep level (Fig. 8c, f), and may be associated with alternating subthermocline zonal jets reported by Qiu et al. (2013).

Figure 9 shows the distribution of the gyre axes at different depths calculated from the appearance rate of the gyre axis and the mean dynamic height maps. The results are almost the same, illustrating a contrast between a large northward shift of the gyre axis to the east of about 180° and a similar but quite small shift to the west. The 180° roughly corresponds to the area where the depth-integrated geostrophic circulation shows a discrepancy with the wind-driven circulation to the west (Sect. 3.1).

The gyre shift can be seen more directly from meridional sections of zonal geostrophic velocity (Fig. 10). The high appearance rate of the gyre axis approximately follows the line of a zero zonal geostrophic velocity, indicating that the climatological gyre axis based on the appearance rate is almost in agreement with the gyre axis of the mean section. In the west at 160°E (Fig. 10a), the gyre axis lies just along the southern flank of a strong barotropic-like eastward jet of the Kuroshio Extension. On the other hand, it is located in a broad weak zonal flow in the east at 160°W (Fig. 10b).

The northward shift of the gyre axis is related to the conservation of PV of the gyre circulation (Stommel and Schott 1977). The conservation of PV gives rise to a decrease in the thickness of a water column to the south, which results in the formation of a clockwise spiral of geostrophic velocity vectors with increasing depth, thus causing the northward shift of the subtropical gyre. Figure 11 shows meridional sections of PV and potential density with the positions of the climatological gyre axis superimposed. Under the assumption of negligible relative vorticity, the PV is calculated between the adjacent depths as follows:

$$\mathrm{PV} = -\frac{f}{\rho}\frac{\Delta\sigma_\theta}{\Delta z}, \tag{3}$$

where $\Delta\sigma_\theta$ is the potential density difference and Δz is the depth interval. It is linearly interpolated into isopycnal surfaces with a 0.05 kg/m^3 interval. The meridional gradients of PV are also computed on isopycnal surfaces.

Two distinct mode waters characterized by low PV less than 2.0×10^{-10} m^{-1}s^{-1} are found around the climatological gyre axis at depths of 200–300 m at 160°E and 200–500 m at 160°W, which correspond to subtropical mode water (STMW; Masuzawa 1969) and CMW, respectively. The STMW and CMW exist widely in the northwestern and central areas of the subtropical gyre, typically in the

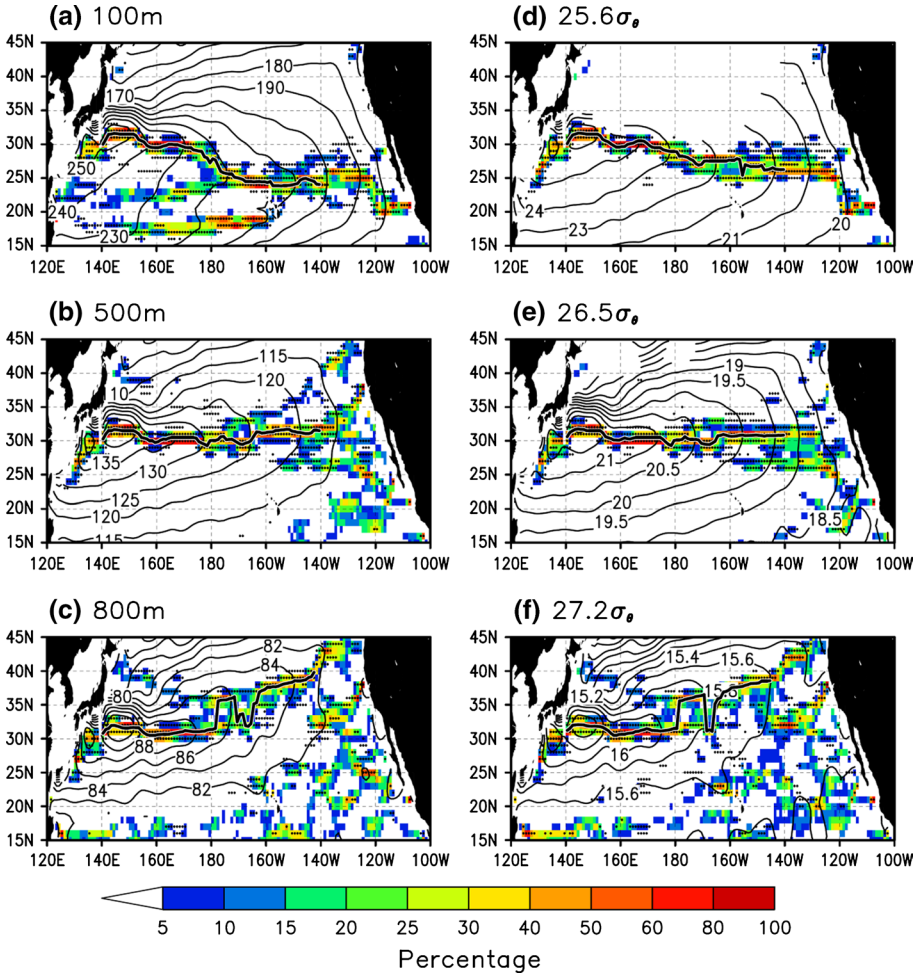

Fig. 8 Mean dynamic heights at **a** 100 m, **b** 500 m, and **c** 800 m depths and acceleration potential on **d** 1025.6, **e** 1026.5, and **f** 1027.2 kg/m^3 density surfaces. *Color* indicates the appearance rates of the gyre axis. *Thick black lines* show the position of the climatological gyre axis determined from the appearance rate (see the text for details). *Black dots* denote the grid points where the appearance rate is statistically significant at the 95th percentile confidence interval

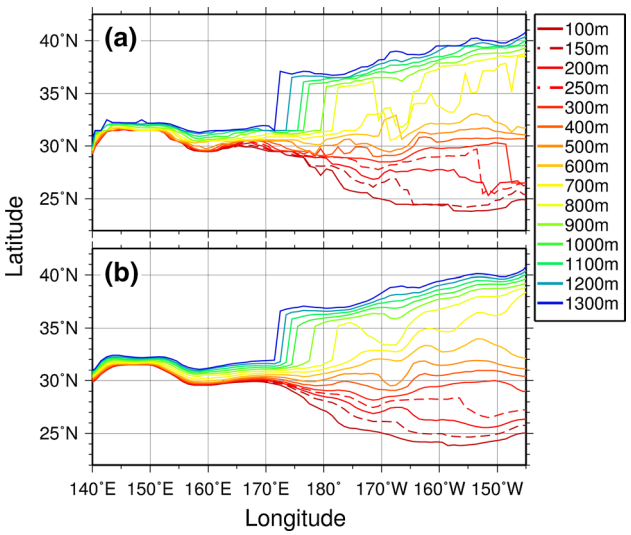

Fig. 9 Distribution of the gyre axis at different depths, determined from (**a**) the rate of appearance of the gyre axis and (**b**) the mean dynamic height maps

density range of 1025.0–1025.6 and 1026.0–1026.5 kg/m^3, respectively (Suga et al. 2004).

At 160°W, the PV on isopycnal surfaces tends to be meridionally uniform in the vicinity of the climatological gyre axis in the lower main pycnocline below the isopycnal surface of about 1026.5 kg/m^3 (Fig. 11d). In the density range between 1025.5 and 1026.5 kg/m^3, above the lower pycnocline, the meridional gradient of PV is generally negative near the climatological gyre axis, indicating that the PV increases to the south. The increase in PV is relatively small in the low PV core of the CMW around 1026.2–1026.5 kg/m^3, but is obvious in the upper pycnocline at the isopycnals of 1025.7–1026.0 kg/m^3 (Fig. 11b, d). Above the isopycnal of 1025.5 kg/m^3, the PV gradient is mostly nearly zero, except it is weak positive just beneath the winter mean sea surface density.

The southward increase of PV near the climatological gyre axis in the east is also recognizable from the climatological mean maps of PV. Figure 12 shows the mean PV and acceleration potential relative to 2000 dbar on the

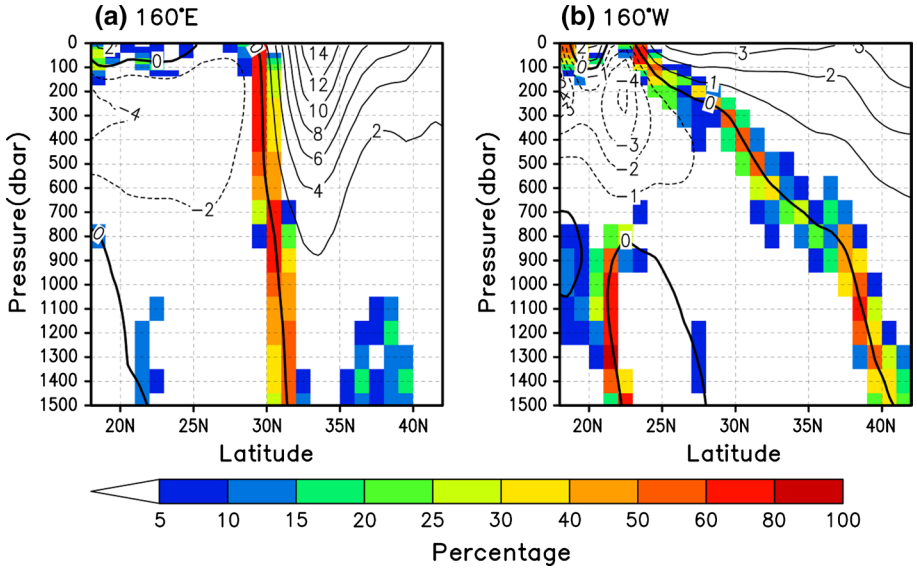

Fig. 10 Meridional sections of the rate of appearance of the gyre axis (*color*) and the zonal geostrophic velocity (cm/s) along (**a**) 160°E and (**b**) 160°W

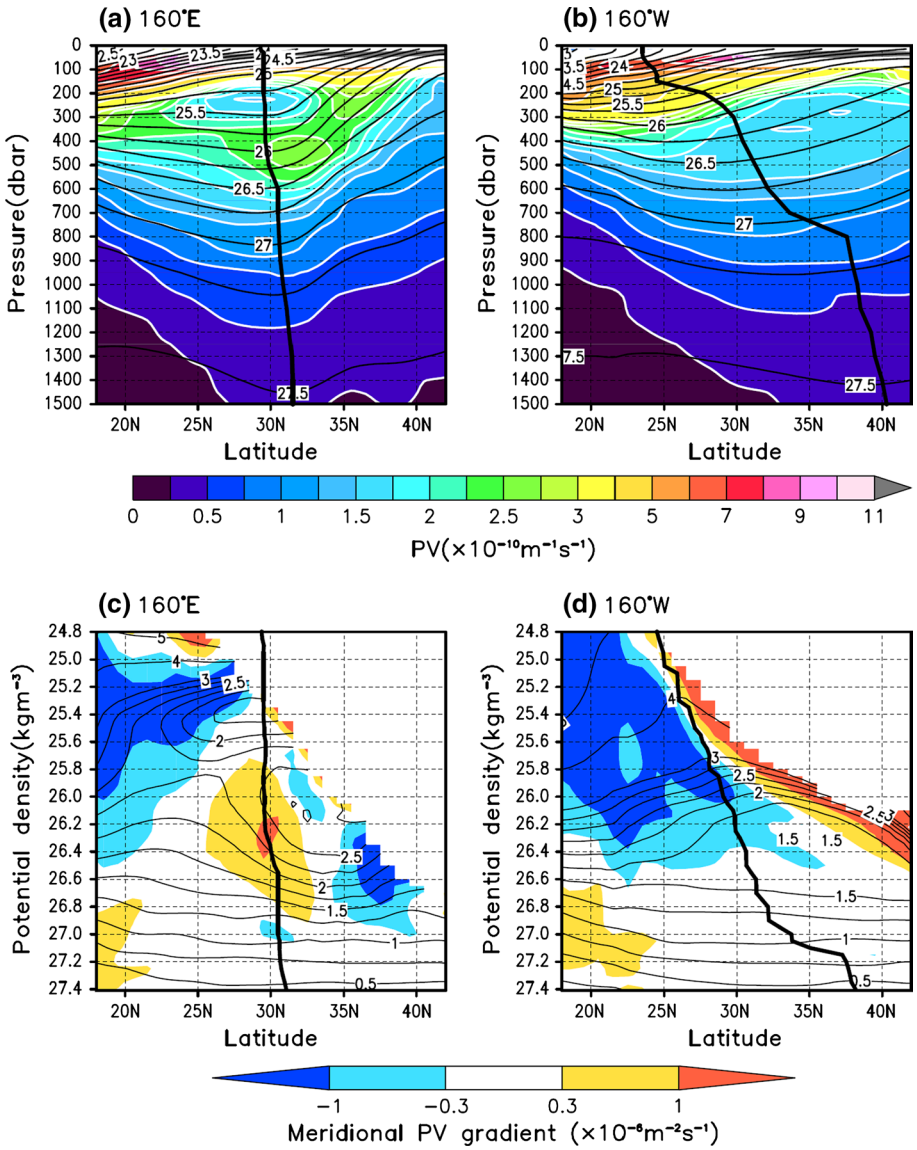

Fig. 11 **a** and **b** Meridional sections of PV (*color*) and potential density (*black contours*), and (**c**, **d**) PV (*black contours*) and its meridional gradient (*color*) on the vertical coordinate of potential density along (**a**, **c**) 160°E and (**b**, **d**) 160°W. *Thick black lines* show the climatological gyre axis. In the *lower panels*, the area where the density is less than the winter sea surface density is masked out

isopycnal surfaces of 1026.0 and 1026.4 kg/m^3. On these surfaces, the CMW appears as a lateral PV minimum to the north of the climatological gyre axis (grey lines in Fig. 12) between 170°W and 160°W, and extends to the south across the climatological gyre axis roughly along the streamlines of the anticyclonic subtropical gyre circulation, forming a tongue-like structure of PV to the southwest. The PV generally increases to the downstream, which is probably due to dissipation by mixing effects of eddies (Xie et al. 2011). Indeed, the changes in PV along the streamlines confirm the general increase to the downstream (Fig. 12c), though it is relatively weak in the lower PV layer of the CMW (blue line in Fig. 12c). These features are also seen from the PV maps shown by Suga et al. (2004) and Kobashi et al. (2006).

At 160°E in the west, the isopycnal PV is relatively uniform near the climatological gyre axis in the STMW layer around 1025.4 kg/m^3 and deep layer below 1026.9 kg/m^3 (Fig. 11c). On the other hand, the PV gradient is positive in the lower main pycnocline between 1025.8 and 1026.8 kg/m^3, indicating a southward decrease of PV, which is in contrast to relatively uniform PV of the lower pycnocline in the east. This decrease in PV to the south is primarily due to relatively high PV water of the pycnocline at depths of 350–700 m (Fig. 11a), which lies in the midst of a strong eastward flow of the Kuroshio Extension (Fig. 10a), suggesting that the pycnocline of the Kuroshio Extension disrupts the meridional continuity of PV. The decrease in PV to the south is also seen from the changes in PV along the acceleration potentials (Fig. 12c). The water in the pycnocline of the Kuroshio Extension first moves to the east and then veers to the southwest, during which the PV gradually decreases. The high PV water in the pycnocline is also clearly identified from the zonal sections of potential density and PV (Fig. 13), displaying that the high PV pycnocline extends to about 180°, approximately in the area where the weak gyre shift with depth is observed.

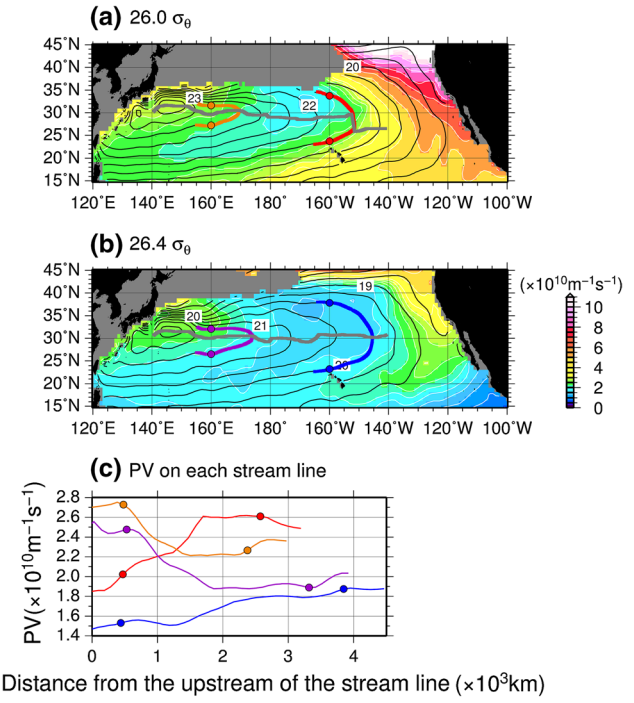

Fig. 12 Maps of mean PV (*color*) and acceleration potential relative to 2000 dbar (*black contours*) on the isopycnal surfaces of (**a**) 1026.0 and (**b**) 1026.4 kg/m^3. *Gray lines* denote the climatological gyre axis. *Light shade* indicates the area with the winter sea surface density that is heavier than each isopycnal. *Red* (*blue*) and *orange* (*purple*) *lines* are the isolines of the acceleration potential of 21.5 (20.0) and 23.5 (21.5) m^{2}s^{-2} on the isopycnal surface of 1026.0 kg/m^3 (1026.4 kg/m^3) across 160°W and 160°E, respectively. **c** Changes in PV along each streamline in **a** and **b**. *Closed circles* are points at the intersection of each streamline with 160°W and 160°E

The thickness of density layers may be straightforward to see the relationship with the gyre shift. In the present study, the thickness (h) is defined as follows:

$$h = \frac{f}{PV} = -\rho \frac{\Delta z}{\Delta \sigma_\theta}. \tag{4}$$

Figure 14 shows the meridional distributions of the thickness on several isopycnal surfaces, which are zonally averaged between 150°E and 170°E and 170°W and 150°W. The gray curves in each panel represent the thickness that would exist when the isopycnal PV is uniform meridionally, and they were calculated by averaging PV within a 2° latitude bin in the vicinity of the climatological gyre axis

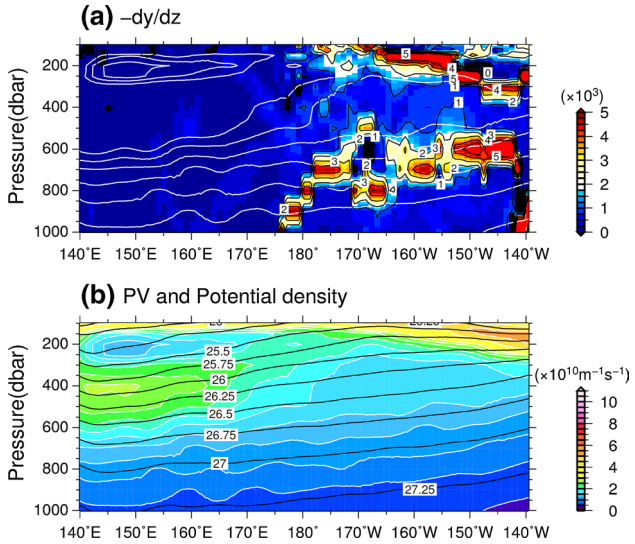

Fig. 13 Zonal sections of (**a**) the change in position of the climatological gyre axis with depth (*color*), and (**b**) PV (*color*) and potential density (*black contours*) averaged between 27.5°N and 32.5°N. *White contours* in the *upper panel* show the PV less than 2 × 10^{-10} m^{-1}s^{-1} with contour intervals of 0.25 × 10^{-10} m^{-1}s^{-1}

on each isopycnal surface and then dividing f by it at each latitude. Therefore, the meridional gradient of the gray curves is β.

As expected from the PV sections in Fig. 11, the thickness of density surfaces in the lower main pycnocline below the isopycnal of 1026.5 kg/m^3 in the east decreases to the south near the climatological gyre axis almost along with β (Fig. 14m, n), because of the uniform PV there. In the CMW layer (Fig. 14j–l), the thickness also decreases to the south, but with larger gradients than β, which especially manifest at 1026.0 and 1026.2 kg/m^3 (Fig. 14j, k), consistent with the southward increase in PV. The southward decreases of thickness are also evident in the upper pycnocline above the CMW (Fig. 14h, i). These results indicate that the thickness of all density layers decreases to the south in the east, favoring the spiral of velocity vectors, and thus the northward shift of the gyre axis.

On the other hand, in the west, the layer thickness shows a southward increase or a nearly constant value near the climatological gyre axis in the main pycnocline between 1025.8 and 1026.8 kg/m^3 (Fig. 14b–f). These features are confined to the vicinity of the climatological gyre axis, suggesting that the strong Kuroshio Extension is a primary cause of the small gyre shift in the west. In fact, the mean map of geostrophic velocity vertically averaged in the upper 2000 m (Fig. 15) demonstrates that the small gyre shift occurs only along the strong Kuroshio Extension.

It is interesting to note that the gyre shift occurs non-uniformly in the vertical in the east (Fig. 11). The northward shift is relatively small near the surface, in the CMW layer between 300 and 500 m depths, and at depths deeper than 900 m, and in contrast, it is large between these layers, equivalently in the upper and lower main pycnoclines. These features are also confirmed from the zonal section of the vertical gradient of the climatological gyre axis (Fig. 13a). The vertical gradient of the climatological gyre axis is calculated from the differences in positions of the climatological gyre axis between the adjacent depths, and the large gradient means a large northward shift of the gyre. Figure 13 clearly displays the small shift in the low-PV CMW layer embedded between the upper and lower pycnoclines.

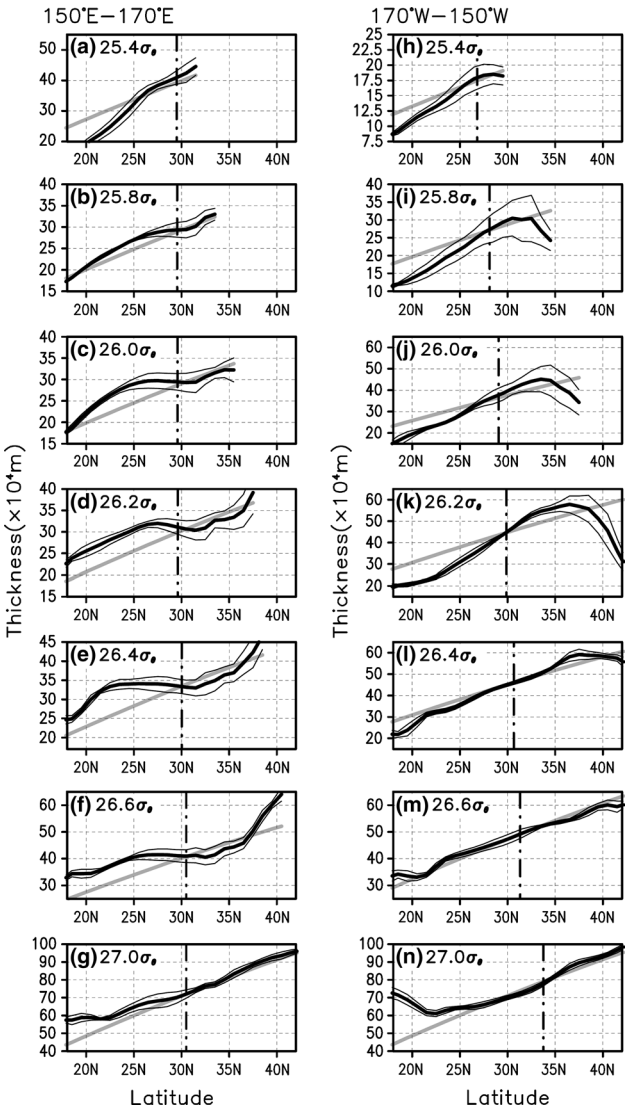

Fig. 14 Meridional distribution of the layer thickness zonally averaged (**a**–**g**) between 150°E and 170°E and (**h**–**n**) between 170°W and 150°W, at **a**, **h** 1025.4, **b**, **i** 1025.8, **c**, **j** 1026.0, **d**, **k** 1026.2, **e**, **l** 1026.4, **f**, **m** 1026.6 and **g**, **n** 1027.0 kg/m^3 surfaces. The *thin black lines* indicate the standard deviation. The *gray lines* show the layer thickness calculated by averaging PV within a 2° latitude bin in the vicinity of the gyre axis and then dividing f into it. The *broken lines* are the position of the climatological gyre axis at the 160°E for **a**–**g** and 160°W for **h**–**m**

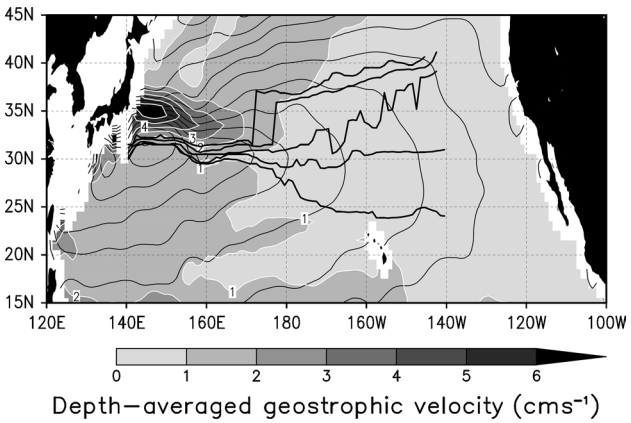

Fig. 15 Depth-averaged geostrophic velocity between the surface and 2000 m (*shade*). The *thin contours* are the mean depth-integrated dynamic heights, the same as in Fig. 1. The *thick black lines* denote the climatological gyre axis at 100, 400, 700, 1000 and 1300 m in Fig. 9a

We investigate the vertical non-uniform shift of the gyre axis, by looking into velocity structure in the vicinity of the gyre axis. Here, we diagnose the observed gyre shift by decomposing it into two components related to vertical and horizontal shears of zonal flow. Since the climatological gyre axis with the high appearance rate is generally in good agreement with the gyre axis of the time mean section (Fig. 10), here we focus on the positions of zero mean zonal velocity as the gyre axis. This enables us to decompose the change in position of the gyre axis with depth (dy/dz), as below:

$$\left.\frac{\mathrm{d}y}{\mathrm{d}z}\right|_{u=0} = -\left.\frac{\partial u}{\partial z}\right|_{u=0} \Big/ \left.\frac{\partial u}{\partial y}\right|_{u=0}, \tag{5}$$

where $\partial u/\partial z$ and $\partial u/\partial y$ are the vertical and horizontal shears of zonal flow, respectively. For convenience, multiplying both sides of the equation by minus, we will refer to the left-hand side ($-$dy/dz) as the change in the gyre axis (positive means a northward shift with depth). This equation means that smaller vertical shear and larger horizontal shear would be related to smaller meridional shift. Figure 16 shows all vertical profiles of these variables between 150°W and 170°W and their averages. The change in the gyre axis (Fig. 16a) captures well two peaks around 250 and 600 m depths in the pycnocline, with a dip between the two peaks.

On which shears is the vertical non-uniformity of the gyre shift dependent? To address this point, we first prepare smoothed profiles of the shears by fitting the mean vertical profile to the following Gaussian function with the least squares method between 100 and 1000 m,

$$\begin{aligned} \frac{\partial u}{\partial z}_{\mathrm{smth}} &= A_1 + B_1 \exp\left(-\frac{z^2}{a_1^2}\right) \\ \frac{\partial u}{\partial y}_{\mathrm{smth}} &= A_2 + B_2 \exp\left(-\frac{z^2}{a_2^2}\right) \end{aligned}, \tag{6}$$

where $A_{1,2}$, $B_{1,2}$, and $a_{1,2}$ are coefficients of the Gaussian function. The results are shown by red lines in Fig. 16b and c. These smoothed profiles produce the gentle shift of the gyre axis with no notable peaks (a red line in Fig. 16a). Then, using these smoothed and original profiles, we calculate two combinations,

$$-\left(\frac{\mathrm{d}y}{\mathrm{d}z}\right)_{\partial u/\partial z} = \frac{\partial u}{\partial z}_{\mathrm{orig}} \Big/ \frac{\partial u}{\partial y}_{\mathrm{smth}}, \tag{7}$$

and

$$-\left(\frac{\mathrm{d}y}{\mathrm{d}z}\right)_{\partial u/\partial y} = \frac{\partial u}{\partial z}_{\mathrm{smth}} \Big/ \frac{\partial u}{\partial y}_{\mathrm{orig}}, \tag{8}$$

where the subscript of the left hand side denotes the variable of the original profile. The results are shown by blue and green lines in Fig. 16a, respectively.

The (dy/dz)∂_u/∂_z shows the two peaks in the pycnocline and the dip between the peaks, reproducing the observed change of the gyre axis. In contrast, though having weak peaks at depths of 200 and 500 m, the (dy/dz)∂_u/∂_y exhibits more gentle change of the gyre axis, which is rather similar to the profile computed from both smoothed shears (see a red line in Fig. 16a). This result indicates that the vertical shear of zonal flow is a major factor for the observed non-uniformity of the gyre shift. Because the vertical shear of zonal flow is related to the meridional gradient of density ($\partial\rho/\partial y$) based on the thermal wind relationship, the large gyre shift in the pycnocline is considered to be due to the large meridional density gradient of the pycnocline and the small shift in the CMW layer is considered to be due to the horizontal uniformity of the CMW. Although the properties of the CMW actually change to the downstream as seen from the PV maps in Fig. 12, the CMW can be still

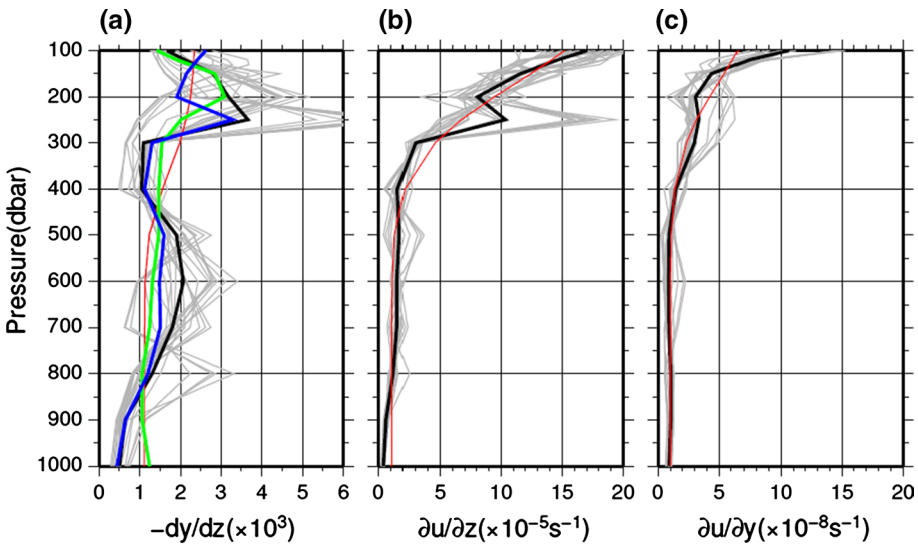

Fig. 16 Vertical profiles of (**a**) the change in position of the gyre axis with depth, (**b**) vertical shears and (**c**) horizontal shears of zonal flow along the gyre axis. *Grey lines* indicate profiles at each longitude between 150°W and 170°W, and *thick black lines* indicate the mean profiles. *Red curves* in **b** and **c** show the smoothed profiles obtained by fitting the mean profile to a Gaussian function, and a *red curve* in **a** is calculated from theses smoothed profiles. *Blue* and *green curves* in **a** indicate the $-$(dy/dz)∂_u/∂_z and $-$(dy/dz)∂_u/∂_y, respectively (see the text for details)

recognized as a relatively uniform water mass from the meridional section in Fig. 11b, and the horizontal changes in density are smaller within the CMW compared to in the main pycnoclines.

4 Summary and discussion

The present study has investigated mean structures of the North Pacific subtropical gyre with a particular focus on the gyre axis, using Argo float observations and several wind stress products. The gyre axes of depth-integrated geostrophic circulation and the vertical structure of the gyre axes both show differences between the regions east and west of about 180°.

Depth-integrated geostrophic circulation shows two gyre axes about 25°N and 30°N in the eastern basin, which correspond well to those of wind-driven circulation. The two gyre axes are created by a local cyclonic wind stress curl anomaly between 145°W and 125°W, probably due to southeasterly wind anomalies there. It is expected from the Sverdrup balance that the two gyre axes would extend further to the west across the subtropical gyre, but the actual geostrophic circulation shows only one gyre axis around 30°N to the west, suggesting some discrepancy with the Sverdrup balance in the west.

Why are the two ocean gyre axes not stretched to the western basin, as expected from the Sverdrup balance? This may boil down to why barotropic Rossby waves forced by the cyclonic wind stress curl anomaly do not propagate to the west. One possible explanation is that Rossby waves actually propagate to the west, but wind-driven circulation is masked by the Kuroshio recirculation gyre, where the transport is dominated by nonlinear dynamics. The recirculation is seen from depth-integrated dynamic height contours veering sharply from the eastward-flowing Kuroshio Extension to the southwest in the region west of about 180° (Fig. 1). The recirculation is characterized by strong barotropic motions with a depth-averaged velocity of about 5–10 cm/s near the south of the Kuroshio Extension (Yoshikawa et al. 2004; Chen et al. 2007), which is much larger than a typical Sverdrup velocity with the order of 0.1 cm/s. Figure 15 shows a large depth-averaged geostrophic velocity in the region south of the Kuroshio Extension west of 180° in comparison to that in the east, though the magnitude of the velocity, about 1–2 cm/s, is much smaller than the observations of Yoshikawa et al. (2004) and Chen et al. (2007), probably due to the spatial smoothing of the MOAA GPV.

The vertical structures of the gyre axis are also quite different between the east and the west of about 180°. The gyre axis shows a prominent northward shift with depth in the east, where a broad weak zonal flow is dominant and the thickness of density layers decreases to the south. On the other hand, in the west, the gyre axis lies just along the southern flank of the strong barotropic-like Kuroshio Extension jet, with no remarkable northward shift. It is suggested that the Kuroshio Extension may disrupt the meridional continuity of PV around the jet, and thus prevent the gyre axis from shifting to the north.

The PV used in the present study does not consider the contribution from relative vorticity. For a large-scale circulation, relative vorticity is reasonably negligible, but in the region of a strong flow such as the Kuroshio Extension, some attention might be needed. Qiu et al. (2006) analyzed CTD and shipboard acoustic Doppler current profiler (ADCP) measurements and pointed out that the inclusion of relative vorticity decreases and increases PV along the southern and northern sides of the Kuroshio Extension jet, respectively, and as a result the PV maximum along the jet is intensified with its position shifted slightly to the north. The effect of relative vorticity disappears immediately away from the jet. Thus, relatively vorticity may not qualitatively change our findings of the southward decrease in PV from the KE region across the gyre axis in the main pycnocline in the west.

Despite the large southward decrease in the thickness of the CMW layers (Fig. 14j–l), the northward shift of the gyre axis is relatively small there. This suggests that, although the southward decrease in the layer thickness is necessary for β spiral and the northward shift of the gyre axis, there are other factors that affect the magnitude of the gyre axis shift. In fact, this study found that smaller shift of the gyre axis is due to the horizontal uniformity of the CMW, which shows dynamical effects of the CMW on the subtropical gyre. Most traditional studies on mode waters may have placed emphasis on their characteristics as a heat reservoir memorizing wintertime ocean–atmosphere interaction (e.g., Hanawa and Sugimoto 2004). In contrast, some recent studies have revealed important dynamic roles of mode waters in ocean circulation, and they show that mode waters can generate a narrow surface jet through the transportation of low PV water (e.g., Kobashi and Kubokawa 2012). The present study may present another way that mode waters can affect large-scale ocean circulations.

It may be interesting to look at temporal changes of the subtropical gyre. Recently, Giglio et al. (2012) reported a change in the orientation of the subtropical gyre from an analysis of Argo float data from 2004 to 2011. They pointed out that the gyre axis on the isopycnal surface of 1026.4 kg/m^3 in the main pycnocline shifts to a more northwest–southeast orientation in 2004/2005 and to a more southwest–northeast orientation in 2008/2009. In addition to the barotropic response to time-varying wind forcings, decadal variations of the CMW (Hosoda et al. 2004; Ladd and Thompson 2002) could change the structure of

the subtropical gyre. More specifically, higher (lower) PV CMW could cause more uniform (non-uniform) northward shift of the gyre axis with depth.

Acknowledgments Comments and suggestions from the editor and anonymous reviewers helped to greatly improve the manuscript. This study is partially supported by Grants-in-Aid for Scientific Research of the Ministry of Education, Culture, Sports, Science and Technology, Japan (22106007, 23340139). The MOAA GPV was obtained from the Japan Agency for Marine-Earth Science and Technology (JAMSTEC) website. The JRA25 wind stress data was obtained from the Japan Meteorological Agency website, the J-OFURO from the J-OFURO website of Tokai University, the NCEP/NCAR and NCEP/DOE data from the NOAA website, and the MERRA from the NASA website. The authors would like to acknowledge these data providers.

References

Aoki K, Kutsuwada K (2008) Verification of the wind-driven transport in the North Pacific subtropical gyre using gridded wind-stress products. J Oceanogr 64:49–60

Chelton DB, Mestas-Nuñez AM (1996) The large-scale, wind-driven response of the North Pacific. Int WOCE Newslett 25:3–6

Chen S, Qiu B, Hacker P (2007) Profiling float measurements of the recirculation gyre south of the Kuroshio Extension in May to November 2004. J Geophys Res 112:C05023. doi:10.1029/2006JC004005

Flament P, Kennan S, Lumpkin R, Sawyer M, Stroup E (1998) The ocean. In: Juvik SP, Juvik JO, Paradise TR (eds) Atlas of Hawai'i. University of Hawaii Press, pp 82–86

Giglio D, Roemmich D, Gille ST (2012) Wind-driven variability of the subtropical north pacific ocean. J Phys Oceanogr 42:2089–2100

Hanawa K, Sugimoto S (2004) 'Reemergence' areas of winter sea surface temperature anomalies in the world's oceans. Geophys Res Lett 31:L10303. doi:10.1029/2004GL019904

Hautala SL, Roemmich D, Schmitz WJ Jr (1994) Is the North Pacific in Sverdrup balance along 24N? J Geophys Res 99:16041–16052

Hellerman S, Rosenstein M (1983) Normal monthly wind stress over the World Ocean with error estimates. J Phys Oceanogr 13:1093–1104

Hosoda S, Xie S-P, Takeuchi K, Nonaka M (2004) Interdecadal temperature variations in the North Pacific central mode water simulated by an OGCM. J Oceanogr 60:865–877

Hosoda S, Ohira T, Nakamura T (2008) A monthly mean dataset of global oceanic temperature and salinity derived from Argo float observations. JAMSTEC Rep Res Dev 8:47–59

Huang RX, Qiu B (1994) Three-dimensional structure of the wind driven circulation in the subtropical North Pacific. J Phys Oceanogr 24:1608–1622

Kalnay E, Kanamitsu M, Kistler R, Collins W, Deaven D, Gandin L, Iredell M, Saha S, White G, Woollen J, Zhu Y, Chelliah M, Ebisuzaki W, Higgins W, Janowiak J, Mo KC, Ropelewski C, Leetmaa A, Reynolds A, Jenne R (1996) The NCEP/NCAR 40-year reanalysis project. Bull Am Meteor Soc 77:437–471

Kanamitsu M, Ebisuzaki W, Woollen J, Yang S-K, Hnilo JJ, Fiorino M, Potter GL (2002) NCEP–DOE AMIP-II Reanalysis (R-2). Bull Am Meteor Soc 83:1631–1643

Kobashi F, Kubokawa A (2012) Review on North Pacific Subtropical Countercurrents and Subtropical Fronts: role of mode waters in ocean circulation and climate. J Oceanogr. doi:10.1007/s10872-011-0083-7

Kobashi F, Mitsudera H, Xie S-P (2006) Three subtropical fronts in the North Pacific: observational evidence for mode water-induced subsurface frontogenesis. J Geophys Res 111:C09033. doi:10.1029/2006JC003479

Kobashi F, Xie S-P, Iwasaka N, Sakamoto TT (2008) Deep atmospheric response to the North Pacific oceanic subtropical front in spring. J Clim 21:5960–5975

Kubokawa A (1999) Ventilated thermocline strongly affected by a deep mixed layer: a theory for subtropical countercurrent. J Phys Oceanogr 29:1314–1333

Kubokawa A, Inui T (1999) Subtropical countercurrent in an idealized ocean GCM. J Phys Oceanogr 29:1303–1313

Kubota M, Yokota H, Okamoto T (1995) Mechanism of the seasonal transport variation through the Tokara Strait. J Oceanogr 51:441–458

Kubota M, Iwasaka N, Kizu S, Konda M, Kutsuwada K (2002) Japanese ocean flux data sets with use of remote sensing observation (J-OFURO). J Oceanogr 58:213–225

Ladd C, Thompson L (2002) Decadal variability of North Pacific central mode water. J Phys Oceanogr 32:2870–2881

Luyten JR, Pedlosky J, Stommel H (1983) The ventilated thermocline. J Phys Oceanogr 13:292–309

Masuzawa J (1969) Subtropical mode water. Deep Sea Res 16:436–472

Munk WH (1950) On the wind-driven ocean circulation. J Meteor 7:79–93

Nakamura H (1996) A pycnostad on the bottom of the ventilated portion in the central subtropical North Pacific: its distribution and formation. J Oceanogr 52:171–188

Nakano H, Suginohara N (2002) A series of middepth zonal flows in the Pacific driven by winds. J Phys Oceanogr 32:161–176

Oka E, Suga T (2005) Differential formation and circulation of North Pacific central mode water. J Phys Oceanogr 35:1997–2011

Onogi K, Tsutsui J, Koide H, Sakamoto M, Kobayashi S, Hatsushika H, Matsumoto T, Yamazaki N, Kamahori H, Takahashi K, Kadokura S, Wada K, Kato K, Oyama R, Ose T, Mannoji N, Taira R (2007) The JRA-25 reanalysis. J Meteor Soc Jpn 85:369–432

Press WH, Teukolsky A, Vettering WT, Flannery BP (1992) Numerical recipes. Cambridge University Press, Cambridge, p 963

Qiu B, Koh DA, Lumpkin C, Flament P (1997) Existence and formation mechanism of the North Hawaiian Ridge current. J Phys Oceanogr 27:431–444

Qiu B, Hacker P, Chen S, Donohue KA, Watts DR, Mitsudera H, Hogg NG, Jayne SR (2006) Observations of the subtropical mode water evolution from the Kuroshio extension system study. J Phys Oceanogr 36:457–473

Qiu B, Rudnick DL, Chen S, Kashino Y (2013) Quasistationary North Equatorial Undercurrent jets across the tropical North Pacific Ocean. Geophys Res Lett 40:2183–2187. doi:10.1002/grl.50394

Qu T (2002) Depth distribution of the subtropical gyre in the North Pacific. J Oceanogr 58:525–529

Reid JL, Arthur RS (1975) Interpretation of maps of geopotential anomaly for deep Pacific Ocean. J Mar Res 33:37–52

Rhines PB, Young WR (1982) A theory of the wind-driven circulation. Part I: mid-ocean gyres. J. Mar. Res. 40:559–596

Rienecker MM, Suarez MJ, Gelaro R, Todling R, Bacmeister J, Liu E, Bosilovich MG, Schubert SD, Takacs L, Kim G, Bloom S, Chen J, Collins D, Conaty A, Silva AD, Gu W, Joiner J, Koster KD, Lucchesi R, Molod A, Owens T, Pawson S, Pegion P, Redder CR, Reichle R, Robertson FR, Ruddick AG, Sienkiewicz M, Woollen J (2011) MERRA:NASA's modern-era retrospective analysis for research and applications. J Clim 24:3624–3648

Sekine Y, Kutsuwada K (1994) Seasonal variation in volume transport of the Kuroshio South of Japan. J Phys Oceanogr 24:261–272

Stommel H (1948) The westward intensification of wind-driven ocean currents. Trans Am Geophys Union 29:202–206

Stommel H, Schott F (1977) The beta spiral and the determination of the absolute velocity field from hydrographic station data. Deep-Sea Res 24:325–329

Suga T, Takei Y, Hanawa K (1997) Thermostad distribution in the North Pacific subtropical gyre: the central mode water and the subtropical mode water. J Phys Oceanogr 27:140–152

Suga T, Motoki K, Aoki Y, Macdonald AM (2004) The North Pacific climatology of winter mixed layer and mode waters. J Phys Oceanogr 34:3–22

Sverdrup HU (1947) Wind-driven currents of a baroclinic ocean; with application to the equatorial currents of the eastern Pacific. Proc Natl Acad Sci 33:318–326

Uda M, Hasunuma K (1969) The eastward subtropical countercurrent in the western North Pacific Ocean. J Oceanogr Soc Jpn 25:201–210

Xie S-P, Liu WT, Liu Q, Nonaka M (2001) Far-reaching effects of the Hawaiian Islands on the Pacific Ocean–atmosphere system. Science 292:2057–2060

Xie S-P, Xu L-X, Liu Q, Kobashi F (2011) Dynamical role of mode water ventilation in decadal variability in the central subtropical gyre of the North Pacific. J Clim 24:1212–1225

Yoshikawa Y, Church JA, Uchida H, White NJ (2004) Near bottom currents and their relation to the transport in the Kuroshio Extension. Geophys Res Lett 31:L16309. doi:10.1029/2004GL020068

Young WR, Rhines PB (1982) A theory of the wind-driven circulation. Part II: Gyre with western boundary layers. J Mar Res 40:849–872